Three-dimensional synthetic turbulence constructed by spatially randomized fractal interpolation

Zhi-Xiong Zhang, Ke-Qi Ding, Yi-Peng Shi, and Zhen-Su She

Phys. Rev. E **84**, 026328 — Published 29 August 2011

DOI: 10.1103/PhysRevE.84.026328

Three dimensional synthetic turbulence constructed by spatially randomized fractal interpolation

Zhi-Xiong Zhang,[1,*] Ke-Qi Ding,[1,†] Yi-Peng Shi,[1,2] and Zhen-Su She[1]

[1] *State Key Laboratory of Turbulence and Complex Systems and College of Engineering, Peking University, Beijing 100871, P.R. China*

[2] *Center for Applied Physics and Technology, Peking University, Beijing 100871, P. R. China*

A spatially randomized fractal interpolation algorithm to construct three dimensional synthetic turbulence from original coarse field is reported. As same as in one dimension case by Ding et al. (Phys. Rev. E 82, 036311, 2010), during the fractal interpolation, positions mapping between large and small scale cubes are chosen randomly and the stretching factors are drawn from log-Poisson random multiplicative process. A linear combination function defined as the base part in fractal interpolation and a theoretical energy spectrum model for fully developed turbulence are introduced into the procedure. Statistical analysis shows that the synthetic field displays some properties very close to the direct numeric simulated field, such as probability distributions of velocity, velocity gradient and velocity increment, the anomalous scaling behavior of the longitude velocity structure functions, which follows SL94 model precisely. And after a short time direct numeric simulation with the synthetic field as initial data, the typical local dynamical structures described by the teardrop shape of Q-R plane for empirical turbulence can be reproduced.

PACS numbers: 47.27.E-, 02.50.Ey, 47.53.+n

I. INTRODUCTION

Generating synthetic turbulence through a method as simple as possible has received considerable attention in recent years. There have been important progresses in applying this kind of turbulent fields in numerical simulations and understanding experimental data [1]. Especially, since abundant empirical observations having been made about the fractality [2–4] in hydrodynamic turbulence, several methods to construct synthetic fields using fractal functions have been proposed [1, 5–8] with different degrees of success in reproducing various characteristics of turbulence.

A remarkable addition to these efforts is the work of Scotti and Meneveau [9, 10]. They introduced a fractal interpolation (FI) algorithm [11] based on an iterated function system (IFS), which is motivated to evaluate the so-called subgrid scale effects which are crucial to derive a self-consistent large eddy simulation (LES) model of turbulence. Later by introducing two different stretching factors based on the former work, Basu *et al.* [12] obtained anomalous scaling exponents for velocity structure functions. Most of these work have a key concept, namely self-similarity, which is one of the common statistical properties of various natural phenomena encompassing a wide range of scales in space or time.

We also notice that Scotti and Meneveau [13, 14] developed a minimal multiscale Lagrangian map approach to synthesize non-Gaussian turbulent vector fields as initial conditions for numerical simulations. Recently, Chevillard *et al.* [15, 16] designed a Recent Fluid Deformation (RFD) closure for the vorticity field based on the mechanics of the Euler equation at short time, which allows an incompressible velocity field to be built that shares many properties with empirical turbulence. Their works also offered good examples for comparing the local structure between synthetic and real turbulence fields (in this paper, the term "real" mainly refers to those data obtained by experiments or direct numeric simulation (DNS)). Moreover, the team of Vassilicos [17, 18] reported some significant experimental investigations on wind tunnel turbulence with high Reynolds number generated by fractal grids. Their works produced new classes of turbulence, which have some unusual properties and may directly serve as new flow concepts for new industrial flow solutions. All of these works indicated that constructing turbulence field is an important issue.

In an earlier paper[19], we found that in real turbulent fields the positions of similar fluctuations at different scales are almost randomly distributed. Therefore, to improve the traditional FI, we proposed a spatially randomized fractal interpolation (SRFI) and demonstrated that the resulting synthetic fields are much closer to real turbulence in one-dimensional (1D) case by introducing the log-Poisson random multiplicative process (RMP). Besides, we applied a so-called energy spectrum modification (ESM) on the synthetic fields to construct those fields which do not obey absolute scaling laws but exhibit the extended scaling similarity (ESS) [20].

Here, we extend the 1D SRFI into a three-dimensional (3D) version by defining a special linear combination function as the base part used in fractal interpolation. At the same time a theoretical energy spectrum model [21] for fully developed turbulence is chosen to implement ESM. Through statistical analysis, it's demonstrated that some statistical properties such as velocity, velocity gradient and velocity increment probability distributions, flatness and scaling behavior of the longitude

* pekingzzx@pku.edu.cn

† Corresponding author: dingkq@gmail.com

velocity structure functions are close to those of DNS fields. In addition, we discuss the deviation of local structures between the synthetic and DNS fields and make a short time DNS using our synthetic field as initial data, which reproduces the typical local dynamical structures described by Q-R plane for fully developed turbulence.

II. FRACTAL INTERPOLATION AND SPATIALLY RANDOM SIMILARITY

The fractal interpolation technique is an iterative affine mapping procedure to construct a synthetic deterministic small-scale field given a few large-scale anchor points [9–12, 19]. A typical 1D FI scheme can be constructed as follows. Let $\mathbf{Y} = \{(x_i, u_i)\}_{i=0}^{n}, n \geqslant 2, x_0 \neq x_n$, be a set of points in $\mathbf{R}^2$, and denote $\Delta x_i = x_{i+1} - x_i, \Delta u_i = u_{i+1} - u_i$. With the proper set of data $\mathbf{Y}$ and the vertical stretching vector $\mathbf{d} = (d_1, \ldots, d_n)^T$, one can associate the hyperbolic IFS: $\{\mathbf{R}^2; W_1, \ldots, W_n\}$, where each W_i is an affine transformation $\mathbf{R}^2 \to \mathbf{R}^2$ given by

$$W_i \begin{pmatrix} x \\ u \end{pmatrix} = \begin{bmatrix} a_i & 0 \\ c_i & d_i \end{bmatrix} \begin{pmatrix} x \\ u \end{pmatrix} + \begin{pmatrix} e_i \\ f_i \end{pmatrix}, \qquad (1)$$

where $a_i = \Delta x_{i-1}/(x_n - x_0)$, $c_i = \Delta u_{i-1}/(x_n - x_0) - d_i(u_n - u_0)/(x_n - x_0)$, $e_i = x_i - a_i x_n$ and $f_i = u_i - c_i x_n - d_i u_n$. For u is usually regarded as a function of x, hereafter, the LHS of Eq. (1) is denoted by $W_i[u](x)$. When $|d_i| < 1, i = 0, 1, \ldots, n$, the operator set $\mathbf{W} = \{W_i | i = 0, 1, \ldots, n\}$ is a contractive mapping over the continuous function space. The infinite iteration of $\mathbf{W}$ generates a fractal function $u_f(x)$ as the fixed point of the mapping which satisfies $u_f(x) = \lim_{m\to\infty} \mathbf{W}^{(m)}[u](x) \equiv \mathbf{W}[\mathbf{W}[\mathbf{W}...\mathbf{W}[u]...]](x)$. Fig. 1 illustrates an example for the first three steps and the 10th iteration of FI process with $n = 2$ and $d_1 = -d_2 = 0.8$, which produces higher and higher resolution by getting values on smaller and smaller scales.

As we can see, the main feature of FI technique is to model the fluctuations on small scale through a given mapping $\mathbf{W}$ from large one, and the fluctuation structures at adjacent small and large scales connected by $\mathbf{W}$ are geometrically similar. Based on this fundamental idea, let us do some expansibility thinking. First, any 1D velocity signal $u(x), x \in [0, 2N\Delta]$ (Δ is the resolved scale or the initial coarse grid size), can be discretized into $2N$ small segments with size Δ and N large segments with size 2Δ. In each segment, the signal can be decomposed into base part and fluctuation part expressed as

$$\begin{cases} u_s = u_{sb} + u_{sf}, \\ u_L = u_{Lb} + u_{Lf}, \end{cases} \qquad (2)$$

where subscripts b and f are denoted to base part and fluctuation part respectively, while s and L are denoted to small and large scale respectively. Then, the fractal mapping W_i in Eq. (1) for the ith small scale segment

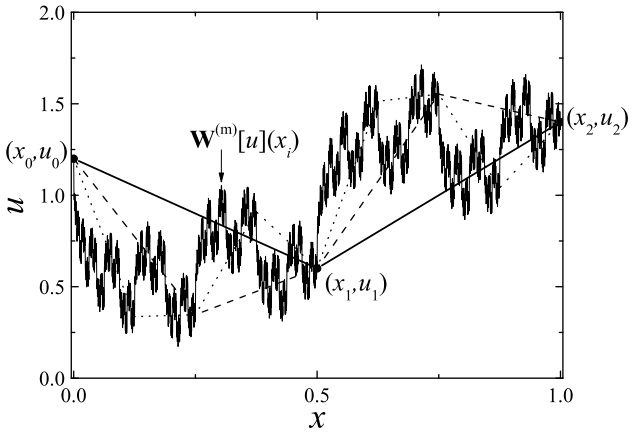

FIG. 1. A demonstration of FI procedure, which interpolates the points (x_0, u_0), (x_1, u_1) and (x_2, u_2). The solid line, dashed line, dotted line and thin line denote $\mathbf{W}^{(0)}[u](x_i)$,$\mathbf{W}^{(1)}[u](x_i)$, $\mathbf{W}^{(2)}[u](x_i)$ and $\mathbf{W}^{(10)}[u](x_i)$, respectively.

with the interval $[x_i, x_{i+1}], x_i = i\Delta, i = 0, 1, \ldots, 2N-1$, can be rewritten equivalently as

$$\begin{cases} W_i[u](x) &= u_{sb}(x) + d_i u_{Lf}(y), \\ y &= M_i(x), \\ x &\in [x_i, x_{i+1}], \end{cases} \qquad (3)$$

where the vertical stretching factor d_i determines the amplitude ratio between similar fluctuations at small and large scales, and M_i describes the preset coordinate/position mapping from corresponding large segment to small one. The interpolation procedure can be sketched by Fig. 2.

Considering Eq. (2) and Eq. (3), we can see three aspects in Fig. 2 need to be defined. The first aspect is how to define the base part or the fluctuation part in subsegment. In early works [9, 10, 12] and in Fig. 1, the base parts u_{sb} and u_{Lb} are defined as linear function pass throigh the anchor points. The second and third aspects are how to set M_i and d_i. For in-

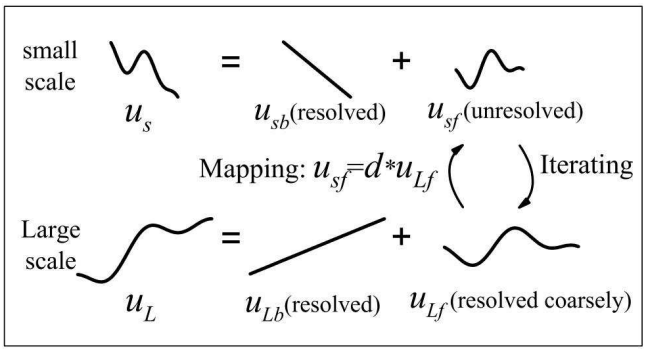

FIG. 2. A sketch for mimicking small scale fluctuations by fractal iteration. Here u_{Lf} is resolved on coarse grid and u_{sf} is unresolved. At each iteration step, u_{sf} is replaced by $u_{sf} = du_{Lf}$, where the stretching factor $|d|$ satisfies $|d| < 1$.

stance, Scotti and Meneveau [9, 10] built their FI scheme by choosing d_i satisfying $|d_i| = 2^{-1/3}$ with a random sign, and setting $M_i(x) = x_i + 2(x - x_i)$ for odd i and $M_i(x) = x_{i-1} + 2(x - x_i)$ for even i. They obtained a turbulence-like field with its fractal dimension equaling to 5/3 and energy spectrum satisfying Kolmogorov $-5/3$ spectrum [22]. Basu *et al.* [12] gave an FI scheme by setting two different stretching factors $d_1 = -0.887$ for odd i and $d_2 = 0.676$ for even i with the same M_i as in Scotti and Meneveau's work. They modeled multi-fractal properties that most turbulent fields possess [23].

With several considerations about above aspects, we extend FI to SRFI. The spatially randomized setting of M_i is the main improvement in SRFI scheme. As we have pointed out in [19], the former FI models assumed that each small scale structure is comprised in the corresponding similar large one, but the spatial relative position of similar fluctuations at different scales is almost randomly distributed in real turbulence. Fig. 3 offers a concrete evident about this feature in a 3D DNS turbulence field with resolution 1024^3. We consider this as one of the most important features of turbulence field. So the locations of similar fluctuations on different scales are modeled randomly with homogeneous distribution in SRFI.

Besides, SRFI has several other improvements, including: choosing the stretching factors d_i randomly with a random sign and the probability of the absolute value obeys a log-Poisson distribution, defining the base part in W_i by a special linear combination function, and even more mimicking the dissipation behavior through an energy spectrum modification. All these arrangements will be detailed in 3D case in the next section. Nevertheless, we want to emphasize that the key concept, namely, the potential of FI or SRFI in constructing turbulence-like field is due to the self-similarity existing in both fractal and turbulence.

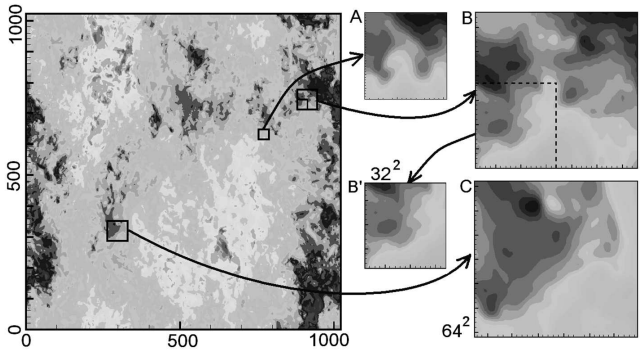

FIG. 3. A section in 3D DNS velocity field with resolution 1024^3. The fluctuations in small square (32^2) A and B' are similar to those in large square (64^2) B and C respectively. Here B' is included in B, but they aren't similar fluctuations. The location relations of similar fluctuations at different scales are provided random.

III. 3D SPATIALLY RANDOMIZED FRACTAL INTERPOLATION

Obviously, 3D SRFI is more complicated than 1D case. One of the main problems is how to define the base and fluctuation part in subsegment, which is in the shape of cubes here. We choose a linear function to solve this problem and transplant the method developed in previous work [19] into 3D case.

For a 3D vector or scalar field $\mathbf{u}(\mathbf{x})$ resolved at scale Δ, we divide the whole region $[0, 2N\Delta]^3$ into $8N^3$ small-scale cubes with each cube size Δ^3,

$$\begin{aligned} K_I &= [x_i, x_{i+1}] \times [y_j, y_{j+1}] \times [z_k, z_{k+1}], \\ &\quad i, j, k = 0, 1, \ldots, 2N-1, \\ I &= i + 2jN + 4kN^2. \end{aligned}$$

Here i,j and k are the indices of the resolved discrete point (x_i, y_j, z_k) in three directions and $I, I = 0, 1, \ldots, 8N^3 - 1$, is the unique index of small-scale cube. The resolved value at point (x_i, y_j, z_k) is denoted by $\widetilde{\mathbf{u}}(i, j, k)$. At the same time, we divide the whole region $[0, 2N\Delta]^3$ into N^3 large-scale cubes with size $8\Delta^3$,

$$\begin{aligned} K'_J &= [x_{2i'}, x_{2i'+2}] \times [y_{2j'}, y_{2j'+2}] \times [z_{2k'}, z_{2k'+2}] \\ &\quad i', j', k' = 0, 1, \ldots, N-1, \\ J &= i' + j'N + k'N^2. \end{aligned}$$

Here $J, J = 0, 1, \ldots, N^3 - 1$, is the unique index of large-scale cube.

Before modeling the unresolved fluctuations, the base parts on small-scale and large-scale cubes need to be defined. For any $\mathbf{x} = (x, y, z)^T \in K_I$ and $\mathbf{x}' = (x', y', z')^T \in K'_J$, we define coefficients $\mathcal{C}$ and $\mathcal{C}'$ as

$$\begin{aligned} \mathcal{C}_{\alpha_1\alpha_2\alpha_3}(\mathbf{x}) &= \frac{(1+\alpha_1 x^*)(1+\alpha_2 y^*)(1+\alpha_3 z^*)}{8}, \\ (x^*, y^*, z^*) &= \frac{2[\mathbf{x}^T - (x_i, y_j, z_k)]}{\Delta} - \mathbf{e}^T, \\ \mathcal{C}'_{\alpha_1\alpha_2\alpha_3}(\mathbf{x}') &= \frac{(1+\alpha_1 x'^*)(1+\alpha_2 y'^*)(1+\alpha_3 z'^*)}{8}, \\ (x'^*, y'^*, z'^*) &= \frac{[\mathbf{x}'^T - (x_{2i'}, y_{2j'}, z_{2k'})]}{\Delta} - \mathbf{e}^T, \end{aligned}$$

where $\mathbf{e}^T = (1, 1, 1)$ and $\alpha_m = \pm 1, m = 1, 2, 3$. We choose linear combinations of the values at the eight vertexes of corresponding cubes to define the base parts $\mathbf{u}_{sb,I}(\mathbf{x})$ and $\mathbf{u}_{Lb,J}(\mathbf{x}')$,

$$\mathbf{u}_{sb,I}(\mathbf{x}) = \sum_{\substack{\alpha_m=\pm 1\\ m=1,2,3}} \mathcal{C}_{\alpha_1\alpha_2\alpha_3}(\mathbf{x})\widetilde{\mathbf{u}}(i+\frac{\alpha_1+1}{2}, j+\frac{\alpha_2+1}{2}, k+\frac{\alpha_3+1}{2}), \tag{4}$$

$$\mathbf{u}_{Lb,J}(\mathbf{x}') = \sum_{\substack{\alpha_m=\pm 1\\ m=1,2,3}} \mathcal{C}'_{\alpha_1\alpha_2\alpha_3}(\mathbf{x}')\widetilde{\mathbf{u}}(2i'+\alpha_1+1, 2j'+\alpha_2+1, 2k'+\alpha_3+1). \tag{5}$$

Such base part will keep the eight vertices resolved values unchanged during the fractal interpolation. From Eq. (2), the fluctuation parts on small-scale cube K_I and large-scale cube K'_J write

$$\begin{aligned} \mathbf{u}_{sf,I}(\mathbf{x}) &= \mathbf{u}(\mathbf{x}) - \mathbf{u}_{sb,I}(\mathbf{x}) \qquad \mathbf{x} \in K_I, \\ \mathbf{u}_{Lf,J}(\mathbf{x}) &= \mathbf{u}(\mathbf{x}) - \mathbf{u}_{Lb,J}(\mathbf{x}) \qquad \mathbf{x} \in K'_J. \end{aligned}$$

Then the three dimensional fractal interpolation operator W_{SRFI} from large-scale cube K'_J to small-scale one K_I has the form

$$\begin{cases} W_{SRFI}[\mathbf{u}](\mathbf{x}) &= \mathbf{u}_{sb,I}(\mathbf{x}) + d_I \mathbf{u}_{Lf,J}(\mathbf{x}'), \\ \mathbf{x}' = M_I(\mathbf{x}) &= (x_{2i'}, y_{2j'}, z_{2k'}) + 2(\mathbf{x} - (x_i, y_j, z_k)), \\ \mathbf{x} &\in K_I, I = 0, 1, \ldots, 8N^3 - 1, \end{cases} \tag{6}$$

where d_I is the stretching factor, and M_I is the location mapping between small-scale and large-scale cubes.

Because in real turbulence there is little correlation between similar fluctuation locations, the index mapping $J(I)$ in $M_I : I \mapsto J$ is chosen randomly. And a restriction on $J(I)$ is imposed so that each cube K'_J maps and only maps to eight different small cubes $K_{I_l}, l = 1, 2, \ldots, 8$. $J(I)$ is set as follows in detail. Let $\mathbf{I}$ denote the set containing all possible choice of I,

$$\mathbf{I} = \{I | I = 0, 1, 2, \ldots, 8N^3 - 1\}.$$

Then, with J passing from 0 to $N^3 - 1$, we randomly choose $I_l, l = 1, 2, \ldots, 8$, from the set $\mathbf{I}$, set $J(I_l) = J$ and then remove I_l from $\mathbf{I}$. As a result, for each J, there are eight, and only eight, I's, $I_l, l = 1, 2, \ldots, 8$, satisfying $J(I) = J$.

As to the stretching factor d_I, like the 1D case, we choose it randomly with random signs and the probability of the absolute value $|d_I|$ obeying the log-Poisson distribution [24, 25]:

$$P\left(|d_I| = \left(\frac{1}{2}\right)^{\gamma} \beta^n\right) = e^{-\lambda}\frac{\lambda^n}{n!}, n = 0, 1, ..., \tag{7}$$

where the parameters λ, γ and β are relative by

$$\lambda = \frac{1 - 3\gamma}{1 - \beta^3} \ln 2.$$

This log-Poisson RMP can illuminate the famous She-Leveque (SL) model verified widely in turbulence [25],

$$\zeta_p = \gamma p + C(1 - \beta^p), \tag{8}$$

where γ, β are parameters in Eq. (7), which measure the degree of intermittency of the field and how singular the most intermittent structure is, respectively, and C is given by $\zeta_3 = 1$. ζ_p is the scaling exponents of the turbulence scaling law [23]

$$S_p(l) \sim l^{\zeta_p}.$$

Here, $S_p(l)$ is the velocity structure function defined by $S_p(l) \equiv \langle |u(x + l) - u(x)|^p \rangle$, l is increment distance, p is the order and $\langle \cdot \rangle$ stands for ensemble average.

Furthermore, since most real turbulence don't obey absolute scaling laws but perfectly obey ESS scaling laws[20, 26], a modification should be introduced into the SRFI algorithm. A simple way is making an ESM in Fourier space on the SRFI synthetic field as follows [19]:

$$\mathbf{u}'(\mathbf{x}) = \mathcal{F}^{-1}\left[\mathcal{F}(\mathbf{u}(\mathbf{x}))\left(\frac{E'(k)}{E(k)}\right)^{\frac{1}{2}}\right]. \tag{9}$$

Here $E(k)$ is the SRFI synthetic field spectrum, and $E'(k)$ is measured from real field or modeled through extrapolating the initial coarse-grained field spectrum using a theoretical formula[21]. The spectrum formula proposed in [13] is also a good choice. $\mathcal{F}$ and $\mathcal{F}^{-1}$ denote Fourier transformation and inverse Fourier transformation, respectively. This method can also be regarded as a simple filter discussed in [27]. Similarly, one can also set the spectrum $E'(k)$ with weaker/stronger viscosity to mimic a field with weaker/stronger dissipation.

Considering $\mathbf{u}'(x)$ may no longer be solenoidal, it is projected to its divergence-free part in Fourier space

$$\hat{\mathbf{u}}(\mathbf{k}) = \mathbf{P}(\mathbf{k}) \cdot \hat{\mathbf{u}}'(\mathbf{k}) \tag{10}$$

to make sure that $\nabla \cdot \mathbf{u} = 0$, where $\mathbf{P}(\mathbf{k})$ is the projection tensor $P_{ij} = \delta_{ij} - k_i k_j / k^2$, and $\mathbf{k}$ is the wavenumber. Now, the construction of a turbulence-like field $\mathbf{u}(\mathbf{x})$ is accomplished.

IV. STATISTICAL ANALYSIS OF 3D SYNTHETIC FIELD

In the following we present statistical analysis of a sample synthetic velocity field generated using the SRFI procedure described in previous section. And we mainly focus on statistical quantities corresponding to scaling behavior of the field in comparison between the synthetic field and DNS data (see Fig. 4). Fig. 4 shows the velocity field component u in the x-direction of the original DNS (a) and the synthetic (b) fields generated by SRFI. One

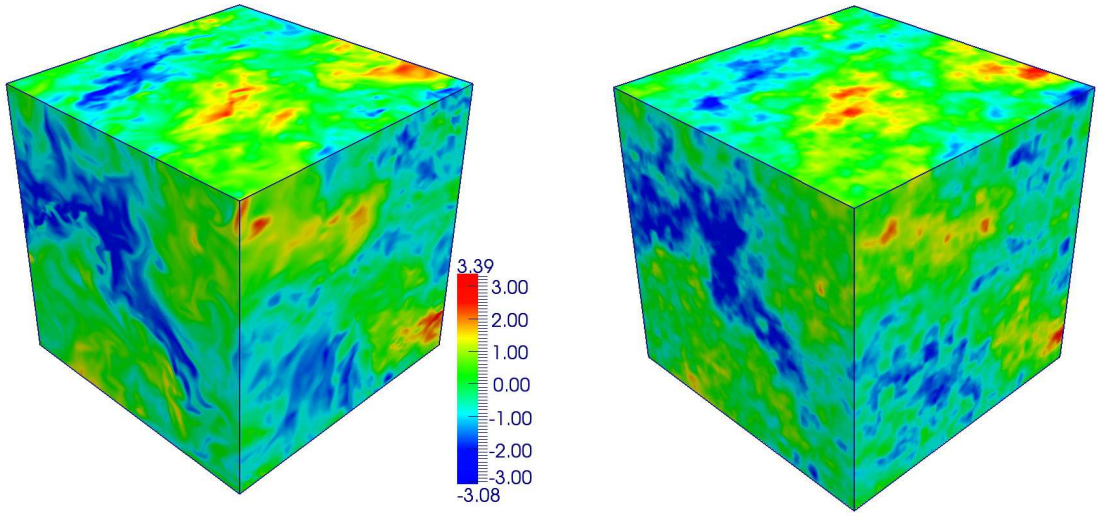

(a)3D DNS field (b)3D SRFI field

FIG. 4. (Color online) Contours of velocity u for (a) the DNS field and (b) this SRFI synthetic field. In both cases u has been normalized by its root mean square (rms) in the respective domain. The figure shows one-eighth of the cube (the octant $[257, 512] \times [257, 512] \times [257, 512]$ of the 512^3 field).

can see that the velocity of synthetic field is close to that of original DNS field though there are still some different structures on small scale.

The main procedure of constructing the synthetic field through SRFI is represented as follows. As the initial resolved field, a coarse velocity field $\tilde{\mathbf{u}}$ with resolution 32^3 is obtained by choosing a point every 16 points in each direction from an original homogenous isotropic turbulence field $\mathbf{u}_0$, which is obtained by DNS with resolution 512^3 and Reynolds number $Re_\lambda = 105$. The DNS is carried out via solving the forced Navier-tokes equations using a pseudospectral code on a cubic box of side $L = 2\pi$ with periodic boundary conditions. More details of the DNS algorithm can be referred to [28, 29]. Thus the setting of $\tilde{\mathbf{u}}$ is approximately equivalent to a low-pass filter with cut-off wavenumber $k_c \sim 10$ (see Fig. 5) and the filter scale is $\Delta = 16\delta$ ($\delta = \pi/256$ is the mesh size of DNS). It should be noted that, choosing the cut-off scale in inertial subrange is very important for reconstructing statistically the typical turbulence scale invariance in the SRFI field.

With parameters $\gamma = 1/9$ and $\beta = (2/3)^{1/3}$ in the log-Poisson distribution Eq. (7) and a random homogeneous distribution for $J(I)$ (M_I) in Eq. (6), the SRFI operator W_{SRFI} is applied on $\tilde{\mathbf{u}}$ four times. The iteration of W_{SRFI} leads to convergence to a fixed point function/field $\mathbf{u}(\mathbf{x})$ with resolution 512^3 and the values at the interpolation points $((x_i, y_j, z_k), i, j, k = 0, 1, \ldots, 2N, N = 16)$ equaling to the given initial resolved values $\tilde{\mathbf{u}}(x_i, y_j, z_k)$.

Then, an ESM is made on $\mathbf{u}(\mathbf{x})$ and the target spectrum in Eq. (9) is modeled by composing that of the initial coarse field ($k \leqslant k_c$) and a universal form proposed in [21] ($k > k_c$),

$$E'(k) = E(k_p)\left[\left(\frac{k}{k_p}\right)^{-5/3} + a\left(\frac{k}{k_p}\right)^{-b}\right] e^{-\mu k/k_p}, \quad (11)$$

with $a = 1.6$, $b = 1.0$ and $\mu = 0.95$. And $k_p = 25$ is the peak wavenumber of the dissipation spectrum and $E(k_p)$ is corresponding energy spectrum value in the original DNS data. After applying a projection to the synthetic field's divergence-free part in Fourier space, the final turbulence-like field is obtained.

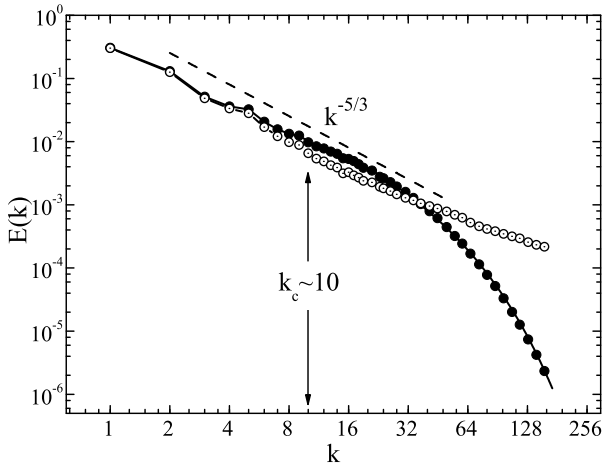

FIG. 5. Log-log plot of the energy spectra of the original DNS(dots), the SRFI(solid line) and the SRFI field before applying ESM(circles) fields. The cut-off wavenumber $k_c \sim 10$ is marked and the Kolmogorov spectrum (dashed line) with slope -5/3 is also plotted as a comparison.

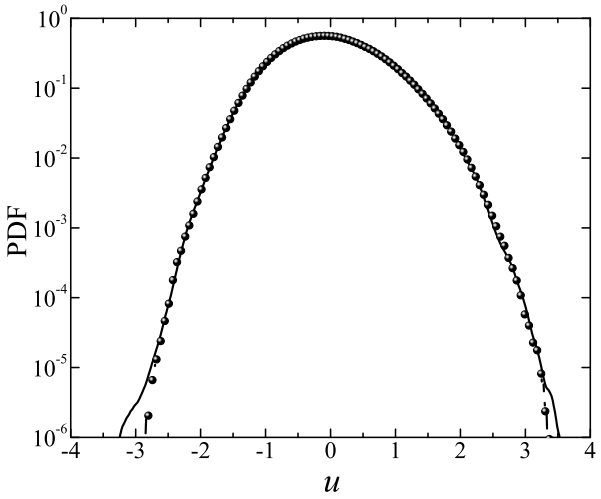

FIG. 6. PDF of velocity u for the SRFI sythetic field (balls) and the original DNS field (solid line).

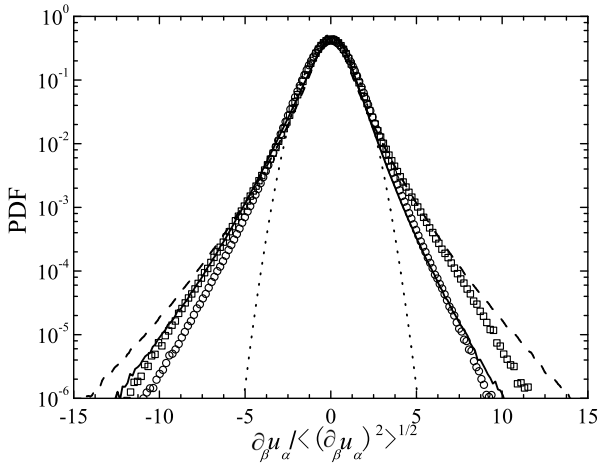

FIG. 7. PDF of velocity derivatives for DNS (lines) and SRFI (symbols) fields. Solid line, circles: longitudinal gradient ($\alpha = \beta$); dashed line, squares: transverse gradient ($\alpha \neq \beta$). Dotted line shows the standard Gaussian PDF.

The main feature of SRFI acting on the velocity field can be illustrated by the spectra shown in Fig. 5. The spectrum of SRFI field before ESM exhibits a straight line in log-log plot, close to the Kolmogorov $k^{-5/3}$ spectrum [22]. This means during SRFI, the information above cut-off scale is preserved and corresponding structure property is transferred to the smaller and smaller scales. Here, to choose the cut-off scale $k_c \sim 10$ in inertial subrange is important. So a scale-invariance cascade without dissipation is mimicked, corresponding to flows with infinity Reynolds number. However, in DNS field at relatively low Reynolds number, the scale-invariance is broken and the spectrum is bent on small scales. Modification need be made on SRFI to capture scaling properties of such DNS data.

Fig. 6 shows the probability distribution function (PDF) of all velocity components in three directions for the synthetic field comparing with DNS result. One can see the velocity distribution is reproduced well enough by interpolating the unresolved points with SRFI method. It also implys our synthetic velocity field resembles the DNS velocity field well, which has been shown in Fig. 4.

Fig. 7 shows the longitudinal and transverse velocity derivatives $\partial_\beta u_\alpha$ in both the synthetic and DNS fields (the plot shows the average of the PDFs for the three longitudinal gradients and the average for the six transverse gradients, which are very similar to each other in both cases). And the PDFs show tendency to form exponential, stretched tails, as well as skewness (asymmetric) for the longitudinal gradient. This turbulence feature has been shown in many data (see, e.g. results from DNS [30–32]). From the figure, we can see there are still some difference between the PDF tails for the synthetic and DNS fields, which maybe the effect of the local structure feature.

Then, let's compare the longitudinal and transverse velocity increments at all scales in both fields. The two kind of velocity increments are defined respectively as

$$\begin{cases} \delta_\parallel u_\alpha(l) &= u_\alpha(\mathbf{x} + l\mathbf{b}^{(\alpha)}) - u_\alpha(\mathbf{x}), \\ \delta_\perp u_\alpha(l) &= u_\alpha(\mathbf{x} + l\mathbf{b}^{(\beta)}) - u_\alpha(\mathbf{x}), \beta \neq \alpha, \end{cases} \tag{12}$$

where $\mathbf{b}^{(\alpha)}$, $\mathbf{b}^{(\beta)}$ are unit vectors in corresponding directions. Fig. 8 and 9 show results for the PDFs of normalized $\delta_\parallel u_\alpha$ and $\delta_\perp u_\alpha$.

Here it is also apparent that the resulting PDFs of this synthetic SRFI field exhibit the analogous behavior (see, e.g., results from DNS [33, 34, 36]). As the separation distance l decreases, the velocity increments statistics deviates increasingly from the Gaussian (approximates to $l/\delta = 256$), and the PDFs present wider tails. Moreover, the transversal increments is almost symmetric often observed in DNS data. The statistical behavior of longitudinal increment is modeled better than that of transversal

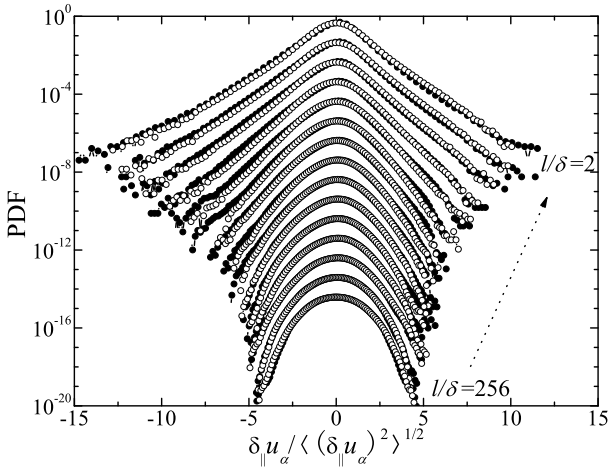

FIG. 8. PDF of normalized longitudinal velocity increments for the SRFI field (filled circles) and the original DNS field (open circles) with separations $l/\delta = 2, 3, \ldots, 256$.

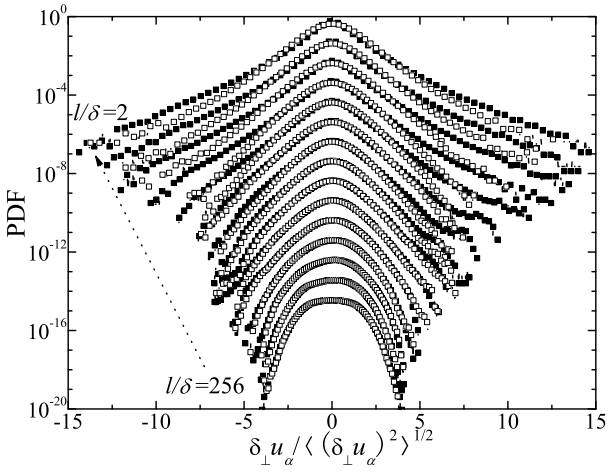

FIG. 9. PDF of normalized transverse velocity increments for the SRFI field (filled squares) and the original DNS field (open squares) with separations $l/\delta = 2, 3, \ldots, 256$.

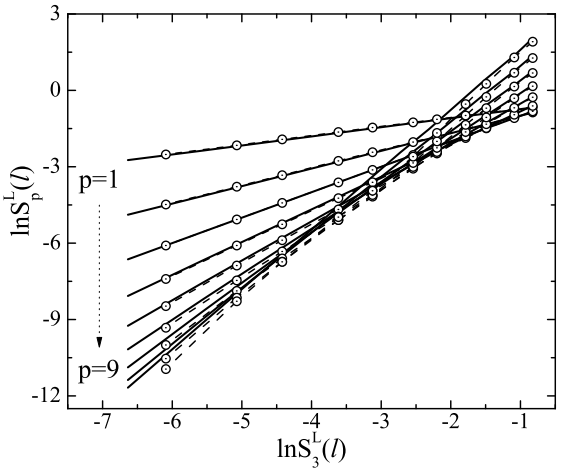

FIG. 11. Longitudinal ESS scaling laws for SRFI field (circles with dash line) and DNS field (solid line). Different lines correspond to orders $p = 1, 2, \ldots, 9$ in the direction of the arrow.

increment, which means the chosen d_I in SRFI is more suitable for longitudinal increment.

Fig. 10 shows the resultant values of skewness and $S(l) = \langle(\delta_\beta u_\alpha)^3\rangle/\langle(\delta_\beta u_\alpha)^2\rangle^{3/2}$ and flatness $F(l) = \langle(\delta_\beta u_\alpha)^4\rangle/\langle(\delta_\beta u_\alpha)^2\rangle^2$ ($\langle\cdot\rangle$ stands for ensemble average, which is replaced by space average in an instantaneous field in this paper without weakening the main conclusions). It is possible to see that the longitudinal increments are skewed in both synthetic and DNS data but the synthetic transversal increment displays weaker intermittent state than the DNS result at small scales. This is a typical character of fractal interpolation, with which the skewness and the flatness can be inherited from coarse scale. And it's difficult to generate obviously stronger intermittency at small scales than at large scales. It also means that skewness and flatness are scale invariant during FI and the corresponding invariables are relative to the initial coarse data.

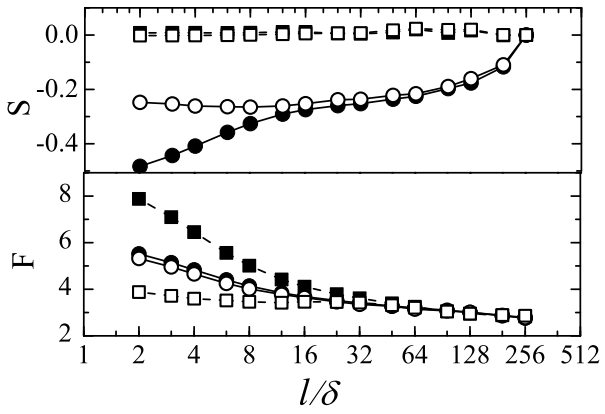

FIG. 10. Skewness (top) and flatness (bottom) coefficients of longitudinal (circles) and transverse (squares) velocity increments as a function of separation distance Δ for the SRFI synthetic (open symbols) and the original DNS fields (filled symbols).

To study the statistical scaling behavior in a field, the key quantities are the velocity structure functions, which are defined as

$$S_p^L(l) = \langle|\delta_\parallel u_\alpha(l)|^p\rangle, \quad S_p^T(l) = \langle|\delta_\perp u_\alpha(l)|^p\rangle. \qquad (13)$$

Fig. 11 and Fig. 12 show the ESS results through the relationship of the longitudinal $S_p^L(l)$ and the transverse $S_p^T(l)$ structure functions with respect to the corresponding third order moment $S_3^L(l)$ and $S_3^T(l)$ for both SRFI synthetic and DNS fields. The two plots demonstrate that the velocity structure functions in both the synthetic field and the original DNS data obey ESS scaling laws precisely. It is also revealed that through SRFI method, the synthetic field's longitudinal ESS properties on small-scale exhibit perfect agreement with DNS data

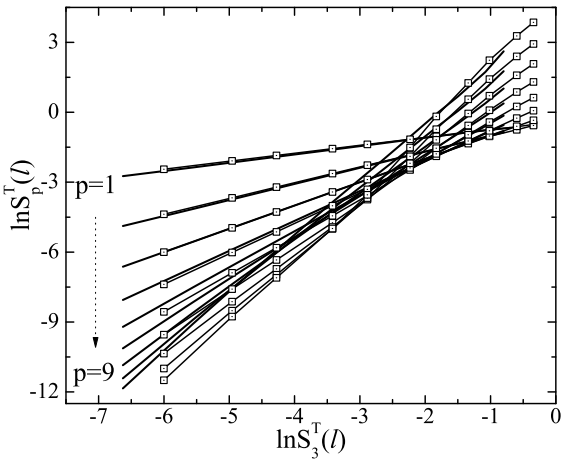

FIG. 12. Transverse ESS scaling laws for SRFI field (squares with dash line) and DNS field (solid line). Different lines correspond to orders $p = 1, 2, \ldots, 9$ in the direction of the arrow.

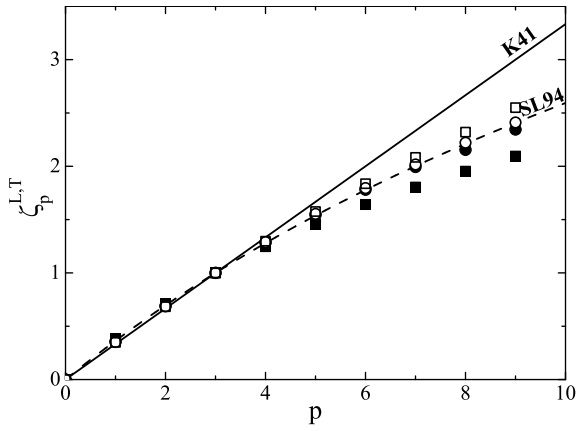

FIG. 13. ESS scaling exponents ζ_p^L (circles) and ζ_p^T (squares) for SRFI field (open symbols) and DNS field (filled symbols). The solid line corresponds to the K41 prediction $\zeta_p = p/3$ and dashed line to SL94 model.

but the transverse ESS properties has obvious deviation, especially at high orders.

Theoretically, using log-Poisson distribution and corresponding parameters used here to set d_I, the scaling exponents of the SRFI field will follow She-Leveque 1994 (SL94) model [35]

$$\zeta_p = p/9 + 2(1 - (2/3)^{p/3}), \tag{14}$$

which is testified in Fig. 13. In the figure, the longitudinal ESS scaling exponents of the synthetic field are in good agreement with the DNS turbulence field and obey the SL94 model; the transverse ESS scaling exponents is also close to SL94 model but deflected from the DNS data; none of them fits the Kolmogorov 1941 (K41) scaling law [22].

We have emphasized in [19], the random affine mapping network in SRFI and the stretching factors with Log-Poisson distribution are essential for constructing a field with anomalous scaling behavior. While Fig. 13 indicates that the transverse scaling behavior is restricted by the log-Poisson random multiplicative process with not suitable parameters. The deviation between ζ_p^L and ζ_p^T can be referred to typical results in [36–38]. In the 3D SRFI scheme proposed here, only one group of parameters can be used. This group parameters support the scaling law described by equation Eq. (14), both in the longitudinal and transverse directions theoretically. But transverse velocity component in typical DNS turbulence does not satisfy this equation even in the initial field. So there are some disagreements between the fractal interpolated results and DNS data. Applying the 1D SRFI separately in the longitudinal and transverse directions (using appropriate spectra) and using two groups of log-Poisson RMP parameters at the same time maybe a good method to capture the right ζ_p^L and ζ_p^T.

From the statistical analysis above, it can be concluded that the synthetic SRFI field exhibits some typical non-Gaussian features similar to the DNS turbulence field, such as PDFs for velocity, velocity gradient and velocity increment, the anomalous scaling behavior of the longitude velocity structure functions, etc. At the same time, some departures from the homogenous isotropic turbulence field should be noticed.

V. DISCUSSION AND CONCLUSION

Like the 1D case, the 3D SRFI scheme builds a random affine mapping network to imitate the geometrical and statistical similarities of turbulence, which are bridges between phenomenological models and quantitative predictions. During the interpolation, a new succinct method for setting the base part of physical quantities in different scale cubes is introduced. The restriction that each cube maps and only maps to eight distinct smaller cubes implies that the probabilities of similar fluctuations at different scales are the same, which leads to the existence of scaling laws.

Though there are many evident successful reproductions of turbulence properties using our 3D SRFI procedure, some differences are also noticed, such as the statistical characteristics of local continuity structure described by some kinds of joint velocity gradient, which is an increasing concern over the past two decades[39].

For example, Fig. 14 illustrates the PDFs for the cosines of the angles between the vorticity vector ω and the eigenvectors $\mathbf{e}^{(1)}, \mathbf{e}^{(2)}, \mathbf{e}^{(3)}$ of the strain-rate tensor $\mathbf{S}$, $S_{ij} = \frac{1}{2}(\frac{\partial u_i}{\partial x_j} + \frac{\partial u_j}{\partial x_i})$, ordered according to their corresponding eigenvalues $\lambda_1 > \lambda_2 > \lambda_3$. These distributions are not so consistent with those in real turbulent flows[40, 41], e.g. the PDFs of $cos(\omega, \mathbf{e}^{(1)})$ and $cos(\omega, \mathbf{e}^{(3)})$ are too close each other.

As another distinct case in point, the invariants Q and R of the velocity gradient tensor $A_{ij} \equiv \partial_j u_i$ are considered with the definitions[42, 43]

$$Q = -\frac{1}{2}A_{ij}A_{ji}, \quad R = -\frac{1}{3}A_{ij}A_{jk}A_{ki}, \tag{15}$$

for incompressible flow. The joint PDF of R and Q normalized by the rate of strain $|\mathbf{S}|^{-1}$ is shown in Fig. 15. The plot depicts contours of probability density spaced logarithmically by factors of 1.6, starting at a value of 0.0001 for the outermost contour. The solid line corresponds to the separatrix $D = \left(\frac{1}{2}R^*\right)^2 + \left(\frac{1}{3}Q^*\right)^3$ (below this separatrix $D < 0$ the eigenvalues of A_{ij} are real, while above it $D > 0$ they are complex [42, 44]). While the symmetrical distribution shows that the plot doesn't represent the teardrop shape observed from DNS data [45, 46] and experimental measurements [47].

The problems above are mainly interrelated with the velocity gradients and their relationship among three directions. One of possible reasons is that the SRFI method proposed here implies a strict succession from large to small scales. So the joint PDF of R and Q at very small scale is the same as that at large scale, which is almost

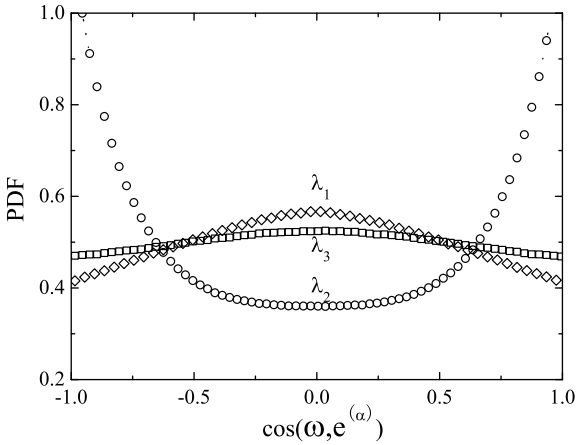

FIG. 14. PDFs of the cosine of the angle between ω and the eigenvectors $\mathbf{e}^{(\alpha)}$ of S_{ij} (corresponding eigenvalues are denoted as λ_α) for the SRFI field. Lozenge: $\mathbf{e}^{(1)}$; squares: $\mathbf{e}^{(2)}$; circles: $\mathbf{e}^{(3)}$.

symmetric, while it has scale dependence in real turbulence [48]. Another reason might be that the SRFI algorithm takes little account of local gradient, thus it is too hard to capture the dynamical tensor correlations.

It is apparent that the dynamical tensor correlations come from the Navier-Stokes equations in essence, so we carried out a standard DNS computing using the SRFI synthetic field as initial conditions. Fortunately, after about one turnover computing time, the modified field has resultant PDFs for $cos(\omega, \mathbf{e}^{(\alpha)})$ and joint PDF of R and Q shown in Fig. 16 and 17, respectively. These distributions are quite consistent with those in real turbulence. It indicates once more that the SRFI synthetic field is a non-Gaussian field which isn't exactly the same but very close to turbulence field.

In conclusion, we have offered a SRFI scheme for constructing a 3D synthetic field sharing many characters with turbulence based on prior works[19], such as PDFs

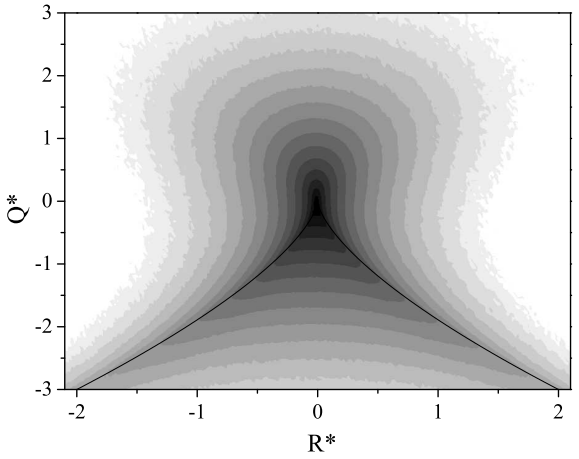

FIG. 15. Joint PDF of the normalized invariants $Q^* \equiv Q/\langle|\mathbf{S}|^2\rangle$, $R^* \equiv R/\langle|\mathbf{S}|^2\rangle^{3/2}$ for the SRFI field. PDF levels are separated logarithmically with the value range $(10^{-4}, 59)$.

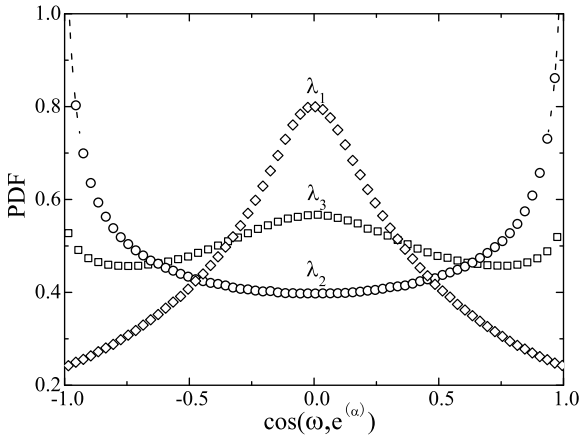

FIG. 16. PDFs in Fig. 14 for the DNS field using the SRFI synthetic field as initial conditions.

for velocity, velocity gradient and velocity increment, and the scaling law of the longitude velocity structure functions. This method is a simple way for generating initial field for massive numeric simulations in the sense of computational time cost reduction. Here, it should also be pointed out, some possible improvements can be imposed on the SRFI method, e.g. applying the 1-D fractal map separately in three different directions like [10] and using two groups of parameters for longitude and transverse quantities, or even replacing velocity with vorticity in SRFI. In addition, using SRFI to establish a sub-scale stress model for large eddy simulation as in [10] and associating SRFI with RFD [16] are also interesting issues. We leave these topics for future investigation.

ACKNOWLEDGEMENT

This work is supported by NSF of China No. 10672004 and No. 90716008, by MOST 973 project 2009CB724100, and by the National Basic Research Programs of China

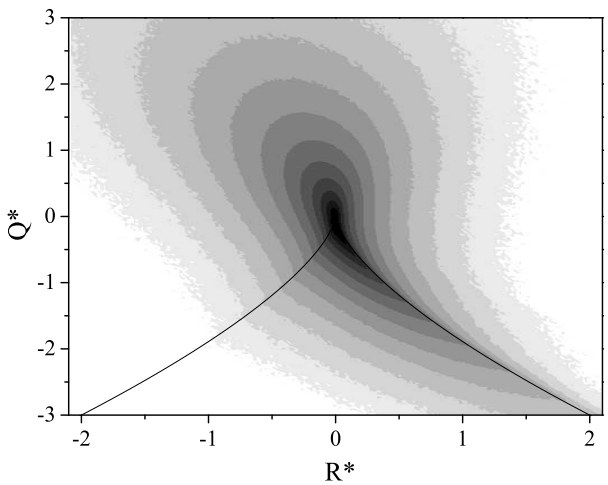

FIG. 17. Joint PDF in Fig. 15 for the DNS field using the SRFI synthetic field as initial conditions.

under Grant No.G2000077305. The authors wish to thank M. Zhou, J. Chen, K. Chen, J. Zhu, N. Hu, X. Shi, J. Pei for helpful discussions, and especially thank N. Hu for offering the Fig. 3.

[1] L. Biferale, G. Boffetta, A. Celani, A. Crisanti, and A. Vulpiani, Phys. Rev. E **57**, R6261 (1998).
[2] J. Feder, *Fractals* (Plenum press, New York, 1988).
[3] C.A.J. Fletcher, *Computational Techniques for Fluid Dynamics* (Springer, New York, 1988).
[4] P. Constantin, I. Procaccia and K.R. Sreenivasan, Phys. Rev. Lett. **67**, 1739 (1991).
[5] T. Vicsek and A. L. Barabási, J. Phys. D **24**, L845 (1991).
[6] R. Benzi, L. Biferale, A. Crisanti, G. Paladin, M. Vergassola, and A. Vulpiani, Physica D **65**, 352 (1993).
[7] A. Juneja, D. P. Lathrop, K. R. Sreenivasan, and G. Stolovitzky, Phys. Rev. E **49**, 5179 (1994).
[8] T. Bohr, M. H. Jensen, G. Paladin and A. Vulpiani, *Dynamical System Approach to Turbulence* (Cambridge University Press, Cambridge, U.K., 1998).
[9] A. Scotti and C. Meneveau, Phys. Rev. Lett **78**, 867 (1997).
[10] A. Scotti and C. Meneveau, Physica D **127**, 198 (1999).
[11] M. F. Barnsley, *Fractals Everywhere* (Academic Press, Boston, 1988).
[12] S. Basu, E. Foufoula-Georgiou, F. Porté-Agel, Phys. Rev. E **70**, 026310 (2004).
[13] C. Rosales and C. Meneveau, Phys. Fluids **18**, 075104 (2006).
[14] C. Rosales and C. Meneveau, Phys. Rev. E **78**, 016313 (2008).
[15] L. Chevillard, C. Meneveau, L. Biferale, and F. Toschi, Phys. Fluids **20**, 101504 (2008).
[16] L. Chevillard, R. Robert and V. Vargas, E.P.L. **89**, 54002 (2010).
[17] D. Hurst and J. C. Vassilicos, Phys. Fluids **19**, 035103 (2007).
[18] N. Mazellier and J. C. Vassilicos, Phys. Fluids **22**, 075101 (2010).
[19] K. Q. Ding, Z. X. Zhang, Y. P. Shi and Z. S. She, Phys. Rev. E **82**, 036311 (2010).
[20] R. Benzi, S. Ciliberto, R. Tripiccione, C. Baudet, F. Massaioli and S. Succi, Phys. Rev. E **48**, R29 (1993).
[21] Z. S. She and E. Jackson, Phys. Fluids. A **5**, 1526 (1993).
[22] A. N. Kolmogorov, Dolk. Akad. Nauk SSSR **32**, 16 (1941)
[23] U. Frisch, *Turbulence, The Legacy of A.N.Kolmogorov* (Cambridge University Press, Cambridge, U.K., 1995).
[24] B. Dubrulle, Phys. Rev. Lett. **73**, 959 (1994).
[25] Z. S. She and E. C. Waymire, Phys. Rev. Lett. **74**, 262 (1995).
[26] R. Benzi, S. Ciliberto, G. Ruzi Chavarria and R. Tripccions, Europhys. Lett. **24**, 275-279 (1993).
[27] S. B. Pope, *Turbulent Flows* (Cambridge University Press, Cambridge, U.K., 2000).
[28] L. P. Wang and M. R. Maxey, J. Fluid Mech. **256**, 27-68 (1993).
[29] L. P. Wang, S. Chen, J. G. Brasseur and J. C. Wyngaard, J. Fluid Mech. **309**, 113-156 (1996).
[30] F. Belin, J. Maurer, P. Tabeling and H. Willaime, Phys. Fluids **9**, 3843 (1997).
[31] T. Ishihara, Y. Kaneda, M. Yokokawa, K. Itakura, and A. Uno, J. Fluid Mech. **592**, 335-366 (2007).
[32] T. Ishihara, T. Gotoh and Y. Kaneda, Ann. Rev. Fluid Mech. **41**, 165-180 (2009).
[33] T. Gotoh, D. Fukayama and T. Nakano, Phys. Fluids **14**, 1065 (2002).
[34] Y. Li and C. Meneveau, Phys. Rev. Lett **95**, 164502 (2005).
[35] Z. S. She and E. Leveque, Phys. Rev. Lett. **72**, 336 (1994).
[36] R. Benzi, L. Biferale, R. Fisher, D. Q. Lamb and F. Toschi, J. Fluid Mech. **653**, 221-244 (2010).
[37] S. Chen, K.R. Sreenivasan, M. Nelkin and N. Cao, Phys. Rev. Lett. **79**, 2253 (1997).
[38] B. Dhruva, Y. Tsuji and K.R. Sreenivasan, Phys. Rev. E. **56**, R4928-R4930 (1997).
[39] J.M. Wallace, Phys. Fluids **21**, 021301 (2009).
[40] K. Ohkitani, Phys. Rev. E. **65**, 046304 (2002).
[41] G. Gulitski, M. Kholmyansky, W. Kinzelbach, B. Lüthi, A. Tsinober and S. Yorish, J. Fluid Mech. **589**, 57-81 (2007).
[42] B.J. Cantwell, Phys. Fluids A **4**, 782 (1992).
[43] B.J. Cantwell, Phys. Fluids A **5**, 2008 (1993).
[44] P. Vieillefosse, Physica A **125**, 150 (1984).
[45] L. Biferale, L. Chevillard, C. Meneveau and F. Toschi, Phys. Rev. Lett. **98**, 214501 (2007).
[46] A. Naso, M. Chertkov and A. Pumir, J. Turbul. **8**, 39 (2007).
[47] F. van der Bos, B. Tao, C. Meneveau, and J. Katz, Phys. Fluids **14**, 2456 (2002).
[48] A. Naso and A. Pumir, Phys. Rev. E. **72**, 056318 (2005).